

Phase-Resolved Observation of Amplitude–Phase Coupling in a Strongly Driven Superconducting Qubit

Kosaku Tabuchi

Hiroshima, Japan

April 15, 2026

Abstract

We report phase-resolved measurements revealing amplitude–phase coupling (APC) in a strongly driven superconducting qubit. Using 1000 shots per point across five drive amplitudes on a Rigetti Ankaa-3 transmon qubit (Qubit 58; $T_1 = 36.7 \mu\text{s}$, $T_2 = 22.2 \mu\text{s}$), we compare a rectangular reference pulse and a self-intersecting Figure-8 trajectory under matched root-mean-square drive amplitude. From harmonic fits to the phase-dependent survival probability, we extract the optimal control phase $\phi^*(A)$ and show that it shifts by more than 3 rad across the explored amplitude range for both pulse families. To quantify phase sensitivity, we define the phase contrast $C(A) = \max_{\phi} \hat{F} - \min_{\phi} \hat{F}$ and the contrast ratio $R(A) = C_{\text{F8}}/C_{\text{Rect}}$. At low amplitude ($A \leq 0.6$), the Figure-8 trajectory reduces phase contrast relative to the rectangular reference ($R = 0.48\text{--}0.57$), whereas at high amplitude ($A \geq 0.8$) it increases it ($R = 1.22\text{--}1.45$), revealing a crossover in trajectory-dependent phase sensitivity. An independent replication acquired in a separate calibration session at 100 shots per point preserves the same low- and high-amplitude sign structure. Additional pulse-train continuity tests show that internal timing gaps reduce phase contrast without measurably shifting the optimal phase, and that a fixed 4 ns gap shows no statistically significant dependence on its placement within the train. Because the comparison is made under matched root-mean-square drive, the residual waveform dependence of the phase landscape is not reducible to a common amplitude-dependent offset alone. These observations identify APC as an experimentally accessible feature of the measured control landscape and show that fixed-phase calibration can become systematically biased across drive amplitudes in the strongly driven regime.

1 Introduction

Achieving robust control in noisy superconducting qubits remains one of the central challenges in near-term quantum computing [1, 2]. Substantial progress has been made in pulse engineering [3, 4], error mitigation [5, 6,

15, 16], and dynamical decoupling and noise-filtering approaches [11, 12, 13, 17] that reduce sensitivity to specific noise channels. Nevertheless, operation in the strongly driven regime remains vulnerable to calibration drift, parameter coupling, and waveform-dependent distortions that are often not captured by standard one-parameter-at-a-time tuning workflows.

In routine calibration practice, drive amplitude, phase, and timing are often treated as approximately independent parameters. This approximation can be adequate in weak-drive settings, but it becomes fragile once strong driving, nonlinear response, and environment-dependent detuning reshape the underlying control landscape [7, 8]. In transmon qubits, for example, amplitude-dependent frequency pulls such as AC Stark shifts are well known to produce phase offsets that vary with drive strength [9, 10]. More recently, it has been shown that in the strongly driven regime the counter-rotating contributions that survive beyond the rotating-wave approximation make the qubit response explicitly dependent on the carrier phase, so that nominally identical operations need not act identically [23]. What is less commonly mapped directly is the *phase landscape* itself: how the phase that maximizes a simple operational observable changes with drive amplitude, and whether that dependence is affected by waveform shape.

In this work we define amplitude–phase coupling (APC) operationally as the dependence of the fitted optimal control phase $\phi^*(A)$ on drive amplitude, with $\phi^*(A)$ extracted from phase-resolved measurements of the survival probability $P(|0\rangle)$. We compare two pulse families under matched root-mean-square drive amplitude: a rectangular reference pulse and a self-intersecting Figure-8 trajectory in the I/Q control plane. Rather than seeking a universal advantage for one waveform, we ask a narrower and more experimentally grounded question: does the measured phase sensitivity change with amplitude, and does that change depend on the chosen trajectory?

The main results are as follows. First, the optimal phase drifts by more than 3 rad across the explored amplitude range for both pulse families, directly revealing APC. Second, the Figure-8 trajectory changes the phase contrast in a regime-dependent way: at low amplitude

it reduces phase contrast relative to the rectangular reference, whereas at higher amplitude the trend reverses. Third, an independent 100-shot dataset acquired in a separate calibration session preserves the same low- versus high-amplitude crossover structure. Finally, supplementary pulse-train continuity tests show that inserting internal timing gaps reduces phase contrast without measurably shifting the optimal phase, and that the effect is insensitive to where a fixed gap is placed within the train. Together, these results support the view that APC is an experimentally accessible feature of the control landscape rather than a purely local timing artifact. Practically, this means that a phase calibration performed at one drive amplitude cannot be assumed to transfer to another in the strongly driven regime, even when the total injected energy is held fixed.

The goal of this paper is therefore limited and operational. We do not attempt to identify a complete microscopic mechanism for APC, nor do we claim a general theory of waveform robustness. Instead, we provide phase-resolved experimental evidence that fixed-phase calibration can become unreliable across drive amplitudes in the strongly driven regime, and that the resulting phase landscape can be measured, compared across pulse families, and used to inform amplitude-aware calibration strategies.

2 Experimental setting and protocol

2.1 Hardware platform

All experiments were performed on Rigetti Ankaa-3, a commercial superconducting quantum processor accessed through Amazon Web Services (AWS) Braket [21]. The target qubit was Qubit 58, a transmon-type qubit. Calibration data recorded at the time of the 1000-shot experiment (2026-03-08) give:

$$\begin{aligned} T_1 &= 36.66 \pm 1.04 \text{ } \mu\text{s}, \\ T_2 &= 22.22 \pm 3.63 \text{ } \mu\text{s}, \\ f_{\text{RB}}^{(\text{iso})} &= 0.99933 \pm 0.00003, \\ f_{\text{RB}}^{(\text{sim})} &= 0.99885 \pm 0.00004, \end{aligned} \quad (1)$$

where $f_{\text{RB}}^{(\text{iso})}$ and $f_{\text{RB}}^{(\text{sim})}$ are the isolated and simultaneous single-qubit randomized-benchmarking fidelities, respectively.

No hardware modification or custom firmware access was used. All control effects reported here arise entirely from software-defined waveform design and timing selection.

2.2 Control trajectories

We compared two pulse families under matched driving conditions. The **rectangular pulse** serves as the reference protocol and is implemented as a constant-direction

drive in the I/Q plane,

$$\begin{aligned} I_{\text{Rect}}(t) &= A \cos \phi, \\ Q_{\text{Rect}}(t) &= A \sin \phi, \end{aligned} \quad (2)$$

for $0 \leq t < T$, with the same loop duration $T = 64$ ns used for the Figure-8 waveform. The **Figure-8 pulse** is a self-intersecting closed trajectory defined by

$$\begin{aligned} I(t) &= A \sin(2\pi t/T + \phi), \\ Q(t) &= A \sin(4\pi t/T + \phi), \end{aligned} \quad (3)$$

where A is the drive amplitude, $T = 64$ ns is the single-loop duration, and ϕ is a common control phase applied to both quadratures. The 2:1 frequency ratio produces a self-intersecting closed loop in the I/Q plane. This waveform was chosen as a simple, software-defined closed trajectory with a single common phase parameter, allowing a controlled comparison against the constant-direction rectangular reference without introducing additional shape parameters. In the present comparison, ϕ is treated operationally as a shared scalar scan parameter for each waveform family; its geometric action in the I/Q plane is not identical for Eqs. (2) and (3), and the comparison is based on the measured response to this shared scan parameter rather than on a strict equivalence of geometric rotation between the two waveform families.

To accumulate measurable phase-dependent modulation while keeping the total pulse train within the qubit coherence window, each waveform was repeated for 50 consecutive loops, giving a total pulse duration of $T_{\text{total}} = 3.2 \text{ } \mu\text{s}$ ($= 64 \text{ ns} \times 50$). The choice of 50 loops should therefore be understood as a practical operating point for resolving phase-dependent modulation within the coherence window, not as a claim of loop-count optimality.

2.3 Isenergetic matching

Comparing two different waveforms requires careful energy matching. We adopted an isenergetic protocol in which the time-integrated microwave energy is equalized between pulse families. For the Figure-8 pulse [Eq. (3)], the root-mean-square (RMS) amplitude over one period is

$$A_{\text{RMS}}^{\text{F8}} = \sqrt{\frac{1}{T} \int_0^T [I(t)^2 + Q(t)^2] dt} = A. \quad (4)$$

The rectangular pulse amplitude was therefore set to the same value $A_{\text{Rect}} = A$, so that the time-integrated energy $\propto \int_0^T [I(t)^2 + Q(t)^2] dt$ is identical for both trajectories at each nominal amplitude point.

This matching reduces differences attributable purely to total injected energy and provides a controlled comparison between waveform families. It does not, by itself, exclude all effects arising from differences in instantaneous power history or higher-order nonlinear response.

2.4 Phase and amplitude scan protocol

The explored amplitudes were $A \in \{0.2, 0.4, 0.6, 0.8, 1.0\}$ in hardware-native arbitrary units. For each amplitude, the control phase was scanned over twelve equally spaced values covering $[0, 2\pi)$. Each experimental shot started from the qubit ground state $|0\rangle$, followed by application of the selected 50-loop pulse train and a final computational-basis measurement. At each (A, ϕ) point, the survival probability $F(A, \phi) \equiv P(|0\rangle)$ was measured using **1000 shots** per point for the primary dataset. An independent replication used 100 shots per point in a separate calibration session on the same qubit. The total primary dataset comprises $5 \times 12 \times 2 = 120$ data points.

2.5 Harmonic fitting and observable extraction

For each $(A, \text{pulse type})$ pair, the phase-dependent data were fitted with a second-order harmonic model:

$$F(A, \phi) \approx c_0 + \sum_{m=1}^2 [a_m \cos(m\phi) + b_m \sin(m\phi)]. \quad (5)$$

All fits achieve $R^2 > 0.986$. From the fitted curve we extract the optimal phase $\phi^*(A) = \arg \max_{\phi} \hat{F}(A, \phi)$, the phase contrast $C(A) = \max_{\phi} \hat{F} - \min_{\phi} \hat{F}$, and the contrast ratio $R(A) = C_{\text{F8}}(A)/C_{\text{Rect}}(A)$.

2.6 Statistical analysis

Error bars for individual data points represent binomial standard errors. Uncertainty in the contrast ratio was assessed by bootstrap resampling (2000 iterations), yielding 95% confidence intervals for $R(A)$ at each amplitude. Because $R(A)$ is reported at five amplitudes, the main text emphasizes effect sizes and bootstrap confidence intervals rather than pointwise null-hypothesis claims. Intervals excluding unity are therefore interpreted descriptively as evidence of separation between waveform families within the measured dataset, while additional details of the supplementary timing tests are provided in the Supplemental Material.

3 Observation of amplitude–phase coupling

Figure 1 shows the phase-resolved survival probability at each drive amplitude for both pulse families. A clear drift of the optimal phase with amplitude is observed. For the rectangular pulse, ϕ^* varies with a total excursion of 3.28 rad (188°). For the Figure-8 trajectory, the excursion is 3.98 rad (228°). This drift directly demonstrates APC.

The extracted optimal-phase paths for the two pulse families are not identical [Fig. 2(a)], indicating that APC is trajectory-conditioned. A purely amplitude-dependent

phase offset that acted identically on both waveform families would be expected to produce more similar phase paths up to a near-constant shift. Instead, the measured paths differ in shape as well as offset, consistent with a waveform-dependent phase landscape in the explored regime.

4 Regime-selective contrast change

Table 1 summarizes the phase contrast and contrast ratio at each amplitude.

Table 1: Phase contrast $C(A)$, contrast ratio $R(A)$, and 95% bootstrap confidence intervals from the 1000-shot dataset.

A	C_{Rect}	C_{F8}	$R(A)$	95% CI
0.2	0.845	0.454	0.537	[0.507, 0.567]
0.4	0.807	0.385	0.477	[0.445, 0.509]
0.6	0.554	0.316	0.571	[0.525, 0.624]
0.8	0.395	0.572	1.447	[1.348, 1.548]
1.0	0.435	0.530	1.219	[1.140, 1.304]

For $A \leq 0.6$, the Figure-8 trajectory reduces the measured phase contrast relative to the rectangular reference: $R(A)$ ranges from 0.477 (52% reduction at $A = 0.4$) to 0.571 (43% reduction at $A = 0.6$), with none of the 95% confidence intervals overlapping unity. For $A \geq 0.8$, the trend reverses, with $R = 1.447$ at $A = 0.8$ and $R = 1.219$ at $A = 1.0$. Both high-amplitude points also have 95% bootstrap confidence intervals that exclude unity.

The phase-resolved scans (Fig. 1) clarify the nature of the contrast reduction: at low amplitudes the Figure-8 trajectory flattens the *entire modulation envelope*, not merely the optimal phase. At higher amplitudes the roles reverse. This rules out a simple phase-shift explanation and indicates that waveform choice changes the measured amplitude–phase response surface itself (Fig. 3).

5 Independent replication

An independent dataset was acquired in a separate calibration session using the same qubit and protocol but with 100 shots per point. Figure 4 compares $R(A)$ between the two sessions. The crossover structure is preserved: $R < 1$ at $A \leq 0.6$ and $R > 1$ at $A \geq 0.8$ in both datasets. All five amplitude points show the same sign of the contrast-ratio effect across sessions.

The quantitative values of $R(A)$ differ between sessions, consistent with the larger statistical noise at 100 shots. The fact that the absolute $\phi^*(A)$ values differ between sessions indicates that the measured APC landscape is session-dependent. Operationally, this means that a phase setting identified in one calibration session need

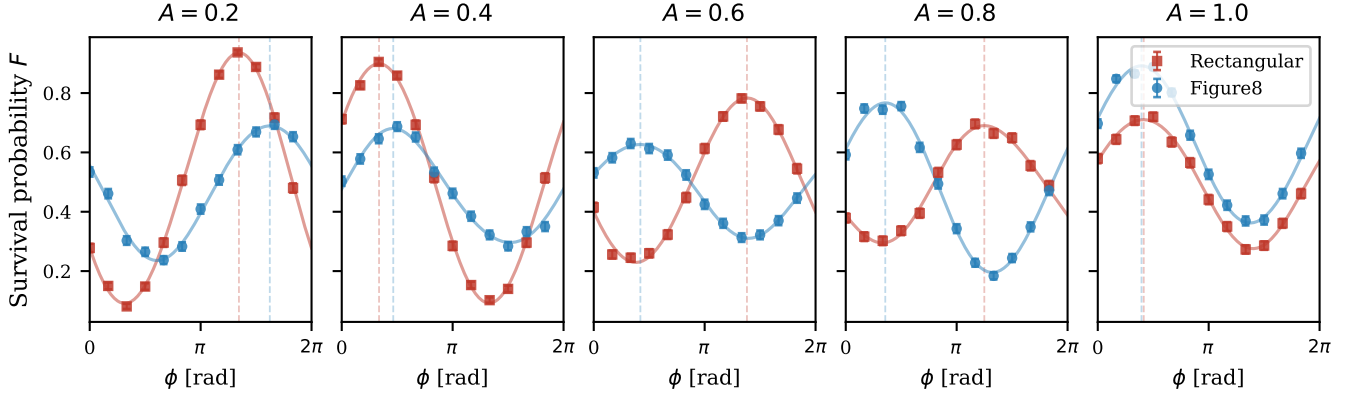


Figure 1: Phase-resolved survival probability at each drive amplitude (1000 shots per point, Qubit 58). Data points with binomial error bars are shown together with second-order harmonic fits for rectangular (red squares) and Figure-8 (blue circles) trajectories. Vertical dashed lines mark the fitted optimal phases $\phi^*(A)$.

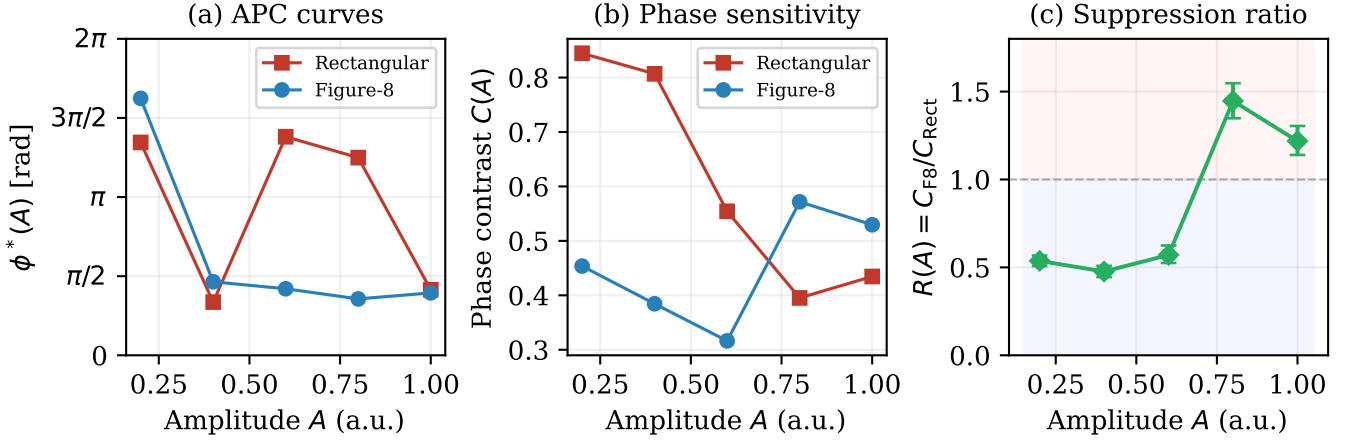


Figure 2: APC summary. (a) Extracted APC curves $\phi^*(A)$. (b) Phase contrast $C(A)$. (c) Suppression ratio $R(A)$ with 95% bootstrap confidence intervals. At every amplitude, the 95% CI lies entirely on one side of unity indicating statistically robust separation within the measured dataset.

not remain optimal in a later session. Such session-to-session variability is consistent with the well-documented temporal instability of superconducting-qubit parameters, which fluctuate on timescales that necessitate frequent recalibration [22].

6 Pulse-train continuity and internal timing

To probe whether the APC landscape reflects a global property of the pulse train or merely a local timing effect, we performed two supplementary experiments using Figure-8 pulses at $A = 0.8$ with 1000 shots per point (see Supplemental Material for pulse-train layouts and supplementary procedural details).

In the first experiment, a controlled idle gap of duration $g \in \{0, 4, 8, 12, 16\}$ ns was inserted at the midpoint of a 25-loop pulse train (12 loops + gap + 13 loops). The gap reduces the phase contrast C from 0.114 at $g = 0$ to 0.067 at $g = 16$ ns, while the optimal phase ϕ^* remains invariant across all gap values. This dissociation—visibility reduction without phase shift—indicates that the gap degrades interference amplitude (consistent with free precession during the idle interval) without altering the underlying phase landscape.

In the second experiment, a fixed 4 ns gap was placed at three different positions within the pulse train (front: 4+21, center: 12+13, back: 21+4) and compared with a no-gap reference. At 1000 shots per point, no measurable dependence on gap position was observed ($\Delta P_0 < 0.013$ across all placements), while the optimal phase remained

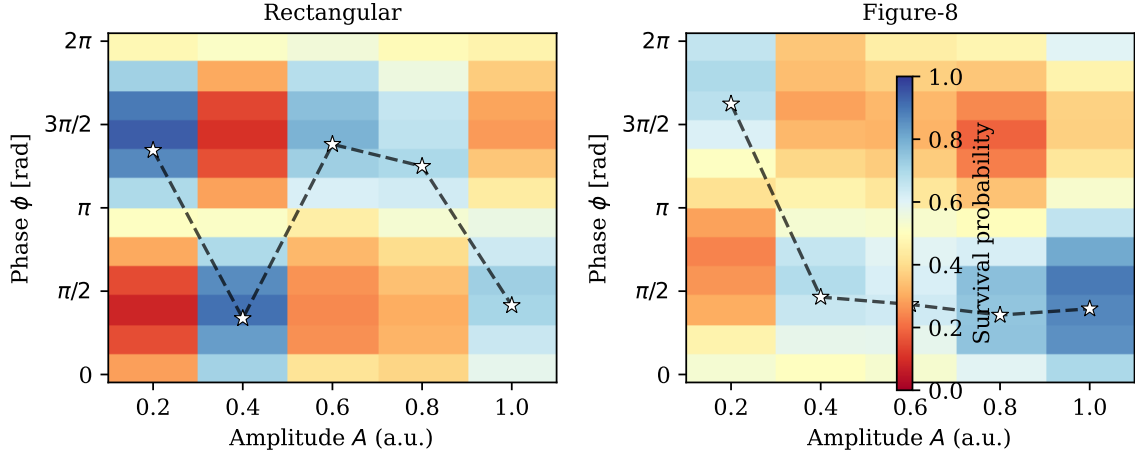


Figure 3: Survival probability in the (A, ϕ) plane for rectangular (left) and Figure-8 (right) trajectories. Dashed curves with star markers trace $\phi^*(A)$.

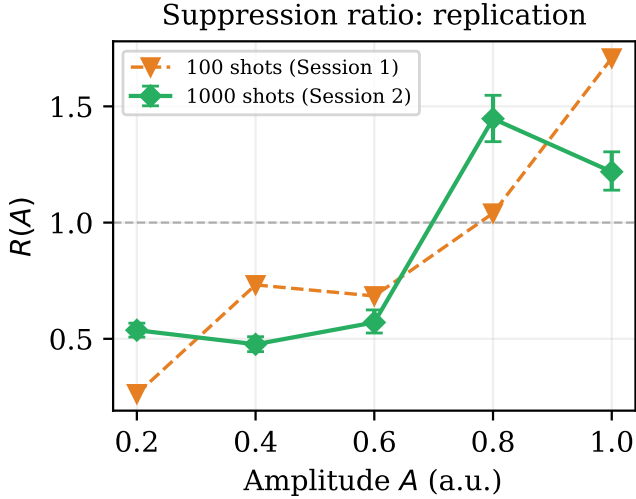


Figure 4: Suppression ratio $R(A)$ from 1000-shot (green, with 95% CI) and 100-shot (orange) sessions. The crossover structure is reproduced.

$\phi^* = 1.55$ rad in all four conditions.

These results support the interpretation that the APC structure is a property of the overall pulse train rather than a purely local timing artifact.

7 Discussion

7.1 Relationship to known amplitude-dependent effects

In transmon qubits, finite-amplitude driving is expected to generate amplitude-dependent detuning and phase offsets through mechanisms such as AC Stark shifts and other nonlinear response effects [9, 10, 7]. In the strongly

driven regime, counter-rotating contributions beyond the rotating-wave approximation are themselves known to introduce carrier-phase-dependent dynamics [23]. Related robust-control and pulse-engineering frameworks have also emphasized the role of waveform-dependent sensitivity to temporally structured noise [19, 20]. A natural question is therefore whether APC is simply a re-labeling of such known amplitude dependence.

The present data support a more limited conclusion. The isenergetic matching of Sec. 2.3 reduces differences attributable purely to total injected energy, yet the rectangular and Figure-8 pulse families still produce distinct $\phi^*(A)$ paths and distinct contrast ratios. This is consistent with APC containing both a waveform-independent amplitude-dependent contribution and an additional waveform-dependent contribution. At the same time, the present experiments do not isolate a unique microscopic mechanism, and they do not exclude the possibility that differences in instantaneous power history, higher-level leakage, or pulse distortion contribute to the observed separation between waveform families. In the strongly driven regime, leakage to higher transmon levels has been characterized in detail and has motivated dedicated optimal-control approaches aimed at suppressing it [18].

This limitation is especially relevant at higher amplitude. Under the present normalization, the rectangular reference has constant instantaneous power $P_{\text{Rect}}(t) = I^2 + Q^2 = A^2$, whereas the Figure-8 waveform has $P_{\text{F8}}(t) = A^2[\sin^2(2\pi t/T + \phi) + \sin^2(4\pi t/T + \phi)]$ and therefore satisfies $P_{\text{F8}}(t) \leq 2A^2$. RMS matching therefore does not imply matched peak power. Dedicated matched-peak comparisons or leakage-sensitive measurements would be required to determine whether the high-amplitude reversal is primarily shape-dependent or instead reflects peak-power-sensitive nonlinearities.

A further observation deserves comment. Even the rectangular reference exhibits a clear phase-dependent response, with a sizeable contrast C_{Rect} at every amplitude

(Table 1). In an idealized resonant rotating-frame description, a constant-phase drive starting from the ground state would be expected to produce no phase-dependent population response at all. The finite C_{Rect} observed here therefore indicates that effects outside such an idealized picture—for example counter-rotating contributions, readout that is not perfectly diagonal in the measurement basis, residual crosstalk, or waveform distortion in the control chain—are present in the measured response. We do not attempt to disentangle these contributions here, but note that they place a natural floor on how literally the contrast ratio $R(A)$ should be read as a comparison of two waveform families.

7.2 Operational interpretation

A microscopic theory is not required for the main operational conclusion of this work. The experimentally relevant observable is the fitted optimal phase $\phi^*(A)$ extracted from phase-resolved measurements of $P(|0\rangle)$. In that sense, APC can be treated as a measured calibration observable: within the explored operating range, the phase setting that maximizes the survival probability depends on amplitude and on waveform family. This conclusion is empirical and does not rely on a particular Hamiltonian-level derivation.

A compact phenomenological picture is still useful. For example, an effective model of the form

$$H_{\text{eff}}(A) = \Omega(A) \sigma_x + \delta(A) \sigma_z, \quad (6)$$

with amplitude-dependent detuning $\delta(A)$ can account for a drifting optimum phase through $\phi^*(A) \sim \arctan[\delta(A)/\Omega(A)]$. We emphasize, however, that Eq. (6) is included only as a phenomenological illustration; it does not explain the full trajectory-dependent crossover in phase contrast.

7.3 Why the contrast change may be regime dependent

The data indicate that the Figure-8 waveform reduces phase contrast at lower amplitudes but increases it at higher amplitudes. One plausible interpretation is that different error channels dominate in different amplitude ranges. At lower amplitude, a slowly varying effective detuning may be the main limitation, making the response comparatively insensitive to details of instantaneous waveform distortion. At higher amplitude, stronger nonlinear detuning, leakage to higher transmon levels, or pulse distortion may become increasingly important and alter the relative behavior of the two waveform families. These mechanisms are consistent with the broader picture established by amplitude-noise spectroscopy [14] and dedicated leakage-control studies in transmon qubits [18]. The present study cannot distinguish among these possibilities, so we report the crossover as an empirical regime dependence rather than a resolved mechanism.

7.4 Implications for calibration

The APC structure implies that fixed-phase calibration can become fragile in the strongly driven regime. A phase setting optimized at one amplitude can become suboptimal at another, and the replication data show that the same is true across calibration sessions. The resulting calibration problem is not purely random, however: within each measured session the optimum phase follows a structured path across amplitude. Operationally, this suggests that amplitude-aware phase calibration can be based on mapped or interpolated phase landscapes within the measured range rather than on a full search at every operating point. The present data do not establish a universal scaling law, but they do indicate that the phase landscape is structured rather than random within each session.

7.5 Scope and limitations

This work does not claim a complete microscopic theory of APC. The present study is limited to a single qubit on a single platform and to a coarse amplitude scan of five operating points. The replication dataset confirms the sign structure of the crossover, but it does not establish cross-platform universality. Distinguishing among possible mechanisms will require denser amplitude scans, explicit leakage-sensitive measurements, additional qubits, and validation on other hardware platforms.

8 Conclusion

We have experimentally identified amplitude-phase coupling in a strongly driven superconducting qubit using phase-resolved measurements of the survival probability. The main findings are as follows.

- (1) The optimal control phase $\phi^*(A)$ drifts by more than 3 rad across the explored amplitude range for both waveform families.
- (2) The Figure-8 waveform changes the measured phase sensitivity in a regime-dependent way: at low amplitude it reduces phase contrast relative to the rectangular reference, whereas at high amplitude it increases it.
- (3) An independent replication acquired in a separate calibration session preserves the same crossover sign structure.
- (4) Supplementary timing tests show that internal gaps reduce phase contrast without measurably shifting ϕ^* , and that a fixed 4 ns gap shows no statistically significant dependence on placement within the pulse train.

Taken together, these results show that the relevant phase landscape in the strongly driven regime can be measured operationally and can differ substantially across waveform families and calibration sessions. Within the scope of the present single-qubit study, the main practical message is that fixed-phase calibration can become unreliable across drive amplitudes, and that amplitude-aware phase mapping within the measured range provides a more informative description of control behavior.

Acknowledgments

Hardware access was provided through AWS Braket.

Data availability

The processed data underlying the figures and the analysis scripts used to extract $\phi^*(A)$, $C(A)$, and $R(A)$ are available at Zenodo: <https://zenodo.org/records/18817369>

References

- [1] J. Preskill, Quantum **2**, 79 (2018).
- [2] P. Krantz, M. Kjaergaard, F. Yan, T. P. Orlando, S. Gustavsson, and W. D. Oliver, Appl. Phys. Rev. **6**, 021318 (2019).
- [3] F. Motzoi, J. M. Gambetta, P. Rebentrost, and F. K. Wilhelm, Phys. Rev. Lett. **103**, 110501 (2009).
- [4] J. M. Gambetta, F. Motzoi, S. T. Merkel, and F. K. Wilhelm, Phys. Rev. A **83**, 012308 (2011).
- [5] K. Temme, S. Bravyi, and J. M. Gambetta, Phys. Rev. Lett. **119**, 180509 (2017).
- [6] Z. Cai *et al.*, Rev. Mod. Phys. **95**, 045005 (2023).
- [7] J. Koch *et al.*, Phys. Rev. A **76**, 042319 (2007).
- [8] H. Ball *et al.*, Quantum Sci. Technol. **6**, 044011 (2021).
- [9] D. I. Schuster *et al.*, Phys. Rev. Lett. **94**, 123602 (2005).
- [10] J. Gambetta *et al.*, Phys. Rev. A **74**, 042318 (2006).
- [11] L. Viola and S. Lloyd, Phys. Rev. A **58**, 2733 (1998).
- [12] K. Khodjasteh and D. A. Lidar, Phys. Rev. Lett. **95**, 180501 (2005).
- [13] M. J. Biercuk, A. C. Doherty, and H. Uys, J. Phys. B **44**, 154002 (2011).
- [14] J. Bylander *et al.*, Nat. Phys. **7**, 565 (2011).
- [15] A. Kandala *et al.*, Nature **567**, 491 (2019).
- [16] S. Endo, S. C. Benjamin, and Y. Li, Phys. Rev. X **8**, 031027 (2018).
- [17] D. A. Lidar, Adv. Chem. Phys. **154**, 295 (2014).
- [18] M. Werninghaus, D. J. Egger, F. Roy, S. Machnes, F. K. Wilhelm, and S. Filipp, npj Quantum Inf. **7**, 14 (2021).
- [19] T. J. Green, J. Sastrawan, H. Uys, and M. J. Biercuk, New J. Phys. **15**, 095004 (2013).
- [20] A. Soare *et al.*, Nat. Phys. **10**, 825 (2014).
- [21] Amazon Web Services, *Amazon Braket Developer Guide* (2024).
- [22] J. J. Burnett, A. Bengtsson, M. Scigliuzzo, D. Niepce, M. Kudra, P. Delsing, and J. Bylander, npj Quantum Inf. **5**, 54 (2019).
- [23] M. F. S. Zwanenburg, S. Singh, E. Y. Huang, F. Yilmaz, T. V. Stefanski, J. Hu, P. Kumaravadivel, and C. K. Andersen, Phys. Rev. Research **7**, 043290 (2025).